Inference of coseismic slip via joint inversion of GPS and aftershock data: The 2004 Parkfield example

A. Ziv[1]

Received 28 March 2011; revised 5 January 2012; accepted 20 January 2012; published 13 March 2012.

[1] In many coseismic slip inversions, the number of model parameters is much larger than that of the independent observations, and the problem is extremely underdetermined. It is thus instructive to incorporate additional data sets into the slip inversion. In this study I describe a new approach for coseismic slip inversion, whereby both GPS displacements and first day aftershock rate changes are used jointly to constrain the solution. The joint inversion incorporates the Dieterich's aftershock model, which adopts a constitutive friction that depends logarithmically on the sliding rate. The method is applied to the 2004 Parkfield earthquake. The joint inversion not only provides resolving power of slip at depths inaccessible to GPS-only inversions, but it also helps to gain insight on the fault mechanical properties. I show that the data are consistent with the adopted aftershock model being the dominant mechanism for aftershock production along the Parkfield segment, and I obtain an upper bound on the friction dependence on the log of rate of fault patches that have experienced aftershock activity. A consequence of the irregular aftershock distribution is that the slip distribution is extremely nonsmooth, with the aftershock zones acting as barriers.

Citation: Ziv, A. (2012), Inference of coseismic slip via joint inversion of GPS and aftershock data: The 2004 Parkfield example, *J. Geophys. Res.*, *117*, B03307, doi:10.1029/2011JB008400.

1. Introduction

[2] Geodetic data are being commonly used to infer coseismic slip distributions. The prime objective of these studies is to identify barriers and/or asperities along the rupture planes [e.g., *Das and Aki*, 1977; *Kanamori and Stewart*, 1978]. This, in turn, may shed light on the rupture physics and help to discriminate between different models [*Du et al.*, 1992; *Fialko et al.*, 2005; *Hsu et al.*, 2006; *Barbot et al.*, 2009].

[3] The standard approach for static slip inversions using geodetic data is to discretize the fault plane into rectangular elements, with each being treated as a dislocation embedded within an elastic half-space. Following spatial discretization and weighting each equation proportionally to the inverse of the data uncertainty squared, the ground displacement, d, due to a permanent slip, u, on the fault surface is

$$W_i G_{ij} u_j = W_i d_i, \tag{1}$$

with W being a weighting matrix and G being Okada's elastic kernel [*Okada*, 1992] for dislocations, relating a unit slip on dislocation j with ground motion at site i. The data contain noise, and that noise is mapped onto the model space. To suppress spurious structure due to noisy data, it is useful to impose smoothing. In this study the smoothing is obtained using [*Mendoza and Hartzell*, 1988]

$$\beta S u_j = 0, \tag{2}$$

where β is a smoothness coefficient and the matrix S is a first difference operator; that is, it sets to zero the slip difference between adjacent cells. Equation (1) subject to the smoothing constraint (2) can then be solved for u using a least squares algorithm.

[4] In many geodetic-only studies, the number of model parameters is much larger than that of the independent observations, and the slip inversion is extremely underdetermined. In such cases, it is instructive to incorporate additional data sets into the slip inversion. In this study I describe a new approach to constrain coseismic slip distribution using both geodetic and aftershock data sets. While it is a common practice to infer the main shock rupture geometry and extent based on the aftershocks spatial distribution, the use of aftershock data to infer the coseismic slip distribution is new [*Bennington et al.*, 2011]. My joint inversion incorporates Dieterich's seismicity rate theory [*Dieterich*, 1994]. The method is applied to the 2004 Parkfield earthquake. By successfully fitting both the GPS and the aftershocks data sets, I show compatibility with the adopted aftershock model. A by-product of the joint inversion is that it provides an upper bound on the friction

[1]Department of Geophysics and Planetary Sciences, Tel Aviv University, Tel Aviv, Israel.

Copyright 2012 by the American Geophysical Union.
0148-0227/12/2011JB008400

dependence on the logarithm of slip speed of fault patches that have experienced aftershock activity.

2. The Joint Inversion Scheme

2.1. The Incorporation of Dieterich's Aftershock Theory

[5] My working hypothesis is that aftershocks occupy areas that experienced coseismic stress increase and that the magnitude of the instantaneous earthquake rate change (defined below) is related to the magnitude of the coseismic stress change. I adopt Dieterich's aftershock model [*Dieterich*, 1994], which employs a constitutive friction coefficient that depends on the logarithm of the sliding speed [*Dieterich*, 1979, 1981].

[6] According to this model, aftershocks occur in response to stress perturbations acting on velocity-weakening fault patches that were near failure before the main shock. This model has been previously implemented to estimate tectonic stressing rate based on the spatial and temporal evolution of Loma Prieta aftershocks [*Gross and Bürgmann*, 1998], to infer stress changes due to dike intrusion in Kilauea volcano in Hawaii [*Dieterich et al.*, 2000], and to infer stress rate change in response to a dike intrusion episode in Izu Islands in Japan [*Toda et al.*, 2002]. In addition, it is being commonly used in probabilistic hazard assessments [*Toda et al.*, 1998; *Parsons et al.*, 2000; *Toda and Stein*, 2002].

[7] An effect that is not accounted for by Dieterich's model is that once an aftershock sequence begins, each aftershock is acting locally as a small main shock by changing the stress field in its surrounding [*Ogata*, 1988; *Helmstetter et al.*, 2003; *Ziv*, 2006a, 2006b]. Consequently, a large fraction of the delayed aftershocks that occur in areas where the stress perturbation caused directly by the main shock is small may be secondary aftershocks, in the sense that they were not triggered directly by the main shock but by earlier nearby aftershocks. Because the use of such aftershocks for the inference of the main shock slip is inappropriate, I attempt to exclude them by counting only those aftershocks that occurred during the first 24 h of the sequence. Therefore, the result of Dieterich's model that is adopted here is the following relation between the coseismic stress change, $\Delta\tau$, and the instantaneous aftershock rate change [*Dieterich*, 1994]:

$$\Delta\tau = a\sigma \ln(R^+/R^-), \tag{3}$$

where a is a constitutive parameter that weights the dependence of the friction coefficient on the logarithm of slip rate, σ is the effective normal stress that I set to be equal to the lithostatic pressure less the hydrostatic pressure, and R^+ and R^- are the postmain shock instantaneous and the premain shock long-term average earthquake rates, respectively. R^+/R^- is resolvable only for areas that were seismically active both before and after the main shock. In fact, it is not uncommon that the spatial distribution of the interseismic microearthquake activity and the aftershock activity are similar, and the 2004 Parkfield earthquake is a good example of that [*Thurber et al.*, 2006]. To obtain a slip distribution that satisfies both the GPS and the aftershock data sets, I solve equations (1) and (2) together with

$$\gamma_\beta K_{lj} u_j = \gamma_\beta \Delta\tau_l, \tag{4}$$

where $\Delta\tau$ is the stress change on seismically active fault patches calculated using equation (3), K is Okada's elastic kernel [*Okada*, 1992] relating a unit slip on j to a stress change on l, where l is the index of the seismically active fault elements for which the R^+/R^- is resolvable. The parameter γ is a relative weight ratio that accounts for the length difference of the two data vectors. If one were to solve equations (1) and (4) using a linear least squares algorithm without appending the smoothing constraint of (2), the relative weight ratio that would result in the two equations having equal weight is

$$\gamma = \frac{\|Wd^{\mathrm{obs}}\|}{\|\Delta\tau^{\mathrm{obs}}\|}, \tag{5}$$

where the superscript "obs" stands for "observed" and the double vertical bars signify the L_2 norm (i.e., the length) of the data vectors. Since here the solution is subject to smoothing and nonnegativity constraints, use of expression (5) does not guarantee equal fit to both data sets. In order to obtain equal fit to the two data sets, I employ a trial-and-error algorithm, where for a given smoothing coefficient, β, I use equation (5) as a starting value for γ_β, which I subsequently adjust to get a slip distribution resulting in equal normalized misfit for the two data sets. The normalized misfit of the ground displacement and the fault stress are defined as

$$\text{normalized misfit} = \frac{\|W(D^{\mathrm{obs}} - D^{\mathrm{est}})\|}{\|WD^{\mathrm{obs}}\|}, \tag{6}$$

where D stands for either ground displacement or fault stress and the superscripts "obs" and "est" signify "observed" and "estimated," respectively. The weight matrix, W, is a unit matrix when D signifies stress.

[8] I constrain the slip to be unidirectional using a nonnegative least squares algorithm [*Lawson and Hanson*, 1974]. Results presented in this study were obtained using Poisson's ratio and Young's modulus that are equal to 0.25 and 70 GPa, respectively.

2.2. Nonuniform Fault Discretization

[9] Typically, model faults are discretized into a few hundreds of elements, say between 200 and 400. While such a discretization may be appropriate for the inversion of ground displacements, it is too coarse for the computation of the on-fault stresses. This is because the stress change near the edge of a slipping element decays proportionally to the inverse of the square root of the distance from that element. Consequently, the stresses at the midpoints of elements closest to a slipping element may be much smaller than the average stress change on these elements. This underestimation of the average stress changes is getting larger with increasing the element's size. To address this issue, I could have refined the grid uniformly up to a level that the grid dimensions are no longer affecting the result. Increasing the number of cells, however, increases both the number of

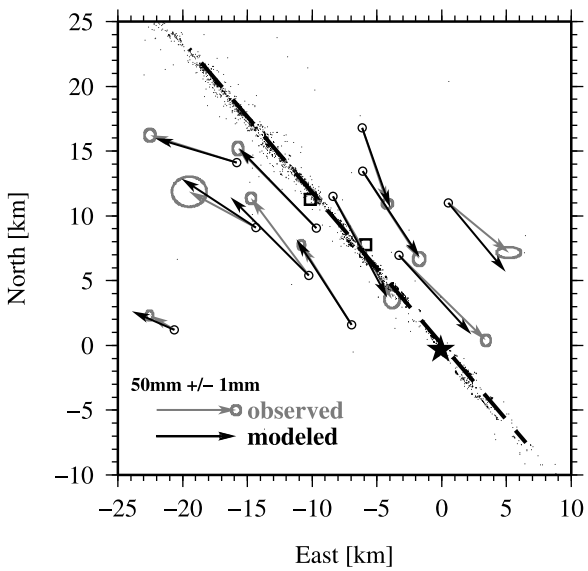

Figure 1. Observed versus modeled coseismic ground displacements. The black circles indicate the 11 GPS sites used in this study, and the two squares indicate the GPS stations excluded from the inversions. Gray and black arrows indicate the observed and modeled horizontal coseismic displacement, respectively. The star shows the 2004 Parkfield epicenter, the grey dots indicate the first day aftershocks [*Thurber et al.*, 2006], and the dashed line indicates the surface trace of the model fault. Uncertainty ellipses indicate 99% confidence level.

model parameters and the size of the elastic kernels. The first effect is undesirable since it renders the inversion even more underdetermined. The disadvantage of the second effect is that a too large elastic kernel is more difficult (or impossible) to invert. Thus here the fault plane is discretized non-uniformly using a quadtree algorithm [*Budiman et al.*, 2007]. That algorithm divides the earthquake rate plot (Figure 2) into four equally sized quadrants and calculates the variance at each quadrant. The quadrant with the highest variance is repeatedly decomposed into four quadrants, until a prespecified number of quadrants is reached. The use of a quadtree algorithm minimizes the differences in the variance of earthquake rate change between adjacent quadrants and results in small cells in areas where aftershock rate is high, and vice versa. After refining the grid within the aftershock zone, where stresses are calculated, the difference between the element midpoint stress and element average stress becomes insignificantly small. Because the observed ground motion is most sensitive to the near-surface slip distribution, quadrants at depths above 4 km were further refined so that their dimensions will not exceed 2.5 by 1 km along the strike and dip directions, respectively.

3. Application to the 2004 Parkfield Earthquake

[10] The available interferometric synthetic aperture radar (InSAR) data for the 2004 M_w 6.0 Parkfield are problematic, as they include contribution from (at least) 2 days of Parkfield unusually large postseismic relaxation [*Johanson et al.*, 2006]. Postmain shock ground displacements caused by afterslip and other relaxation mechanisms can be excluded by using continuous GPS-only displacements, but such slip inversions are extremely underdetermined. Thus, despite being one of the best recorded earthquakes to date, the inference of the 2004 M_w 6.0 Parkfield's coseismic slip distribution using geodetic data is difficult and subject to large uncertainties, and the incorporation of additional data sets into its slip inversion is of great importance [e.g., *Custódio et al.*, 2009; *Bennington et al.*, 2011].

3.1. The Data

[11] The ground displacements associated with the 2004 Parkfield earthquake were monitored by the SCIGN network, which includes thirteen 1 Hz GPS stations near Parkfield (Figure 1). The 1 day static displacements used in this study were computed by the Scripps Orbit and Permanent Array Center (http://sopac.ucsd.edu). Owing to the scarceness of aftershocks above 3 km, the rupture geometry near the surface is poorly resolved. In addition, detailed mapping of fault breaks along the San Andreas within hours of the main shock reveals that a substantial portion of the near-surface slip occurred along secondary faults, mainly along the Southwest Fracture Zone [*Rymer et al.*, 2006]. Thus, the use of a single perfectly straight fault plane to model slip using ground displacements measured within the fault zone is inappropriate [see also *Murray and Langbein*, 2006]. For these reasons I choose to disregard data from two the two GPS sites, whose distance to the model plane is the smallest (indicated by the squares in Figure 1).

[12] The use of instantaneous aftershock distribution for the inference of slip distribution is only sensible if the microearthquake locations are accurate both before and after the main shock. Such is the case with the *Thurber et al.* [2006] double-difference earthquake catalogue that I use in this study. Inspection of this catalog shows that the microearthquake activity along the Parkfield segment is concentrated along subhorizontal streaks, whose position is stationary through time. Many of the microearthquakes within the streaks are repeating earthquakes in the sense their rupture areas occupy fault patches that failed several times, released similar seismic moment and produced nearly identical wavefield each time [*Nadeau et al.*, 1995; *Nadeau and Johnson*, 1998]. *Nadeau and Johnson* [1998] and *Chen and Lapusta* [2009] suggest that the repeating earthquakes rupture stick-slip patches within an otherwise aseismically creeping portion of the fault, whereas *Sammis and Rice* [2001] propose that they occur along the border between locked and aseismic fault patches. Both models imply that these streaks experienced little slip and acted as asperities during the rupture of magnitude 6 earthquakes. It thus appears that the application of the Dieterich aftershock model to the Parkfield segment is appropriate.

[13] Instantaneous aftershock rate change was calculated for $M \geq 1.5$ earthquakes and obtained by dividing aftershock rate during the 24 h after the Parkfield earthquake by the earthquake rate during the 20 years preceding that earthquake on a grid of 300 elements, whose dimensions are 2 by 1 km along the strike and dip directions, respectively. The final earthquake rate diagram shown in Figure 2 is the result of bicubic interpolation between the midpoints of that grid.

[14] Another, much more complete, seismicity catalog that I could have used is that of *Peng and Zhao* [2009], who used

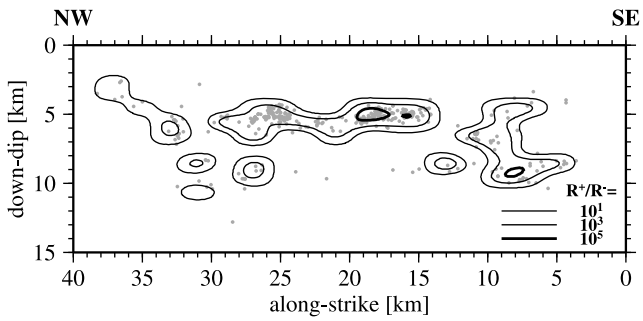

Figure 2. Aftershock rate change. The ratio between the number of first day aftershocks and 20 year background seismicity, calculated for $M \geq 1.5$. Grey dots indicate the double-difference locations of the first day aftershocks. Aftershock rate change was first calculated on a grid of 300 cells, whose horizontal and vertical dimensions are 2 and 1 km, respectively, and then smoothed using bicubic interpolation.

a matched filter technique to identify aftershocks that were masked by the coda of earlier aftershocks listed in the standard catalog of the North California Seismic Network. While the Peng and Zhao catalog contains slightly more than twice the number of magnitude 1.5 and greater earthquakes listed in the *Thurber et al.* [2006] double-difference catalog, the accuracy of their hypocenter locations is not as good. Yet, the overall spatial distribution of aftershocks of the two catalogs is rather similar, and therefore the aftershock rate diagram that I would have obtained had I used the Peng and Zhao catalog would have been similar to the one shown in Figure 2, but with aftershock rate changes that are slightly more than twice larger. I discuss consequences of underestimating the aftershock rate change in section 3.3.

3.2. Model Fault and Resolution

[15] On the basis of precisely located aftershocks, I set the strike and dip of the model fault to be equal to 319.5° and 90°, respectively, and set its along-strike and downdip dimensions to be equal to 40 and 15 km, respectively. After fixing the model fault plane geometry, the problem may be treated as a linear inverse problem and may be formulated as $d = Am$, with d and m being the data and solution vectors, respectively, and the matrix A is the model operator. Because here the dimension of m is smaller than that of d, the inversion is ill-conditioned, and it is important to inspect the resolution matrix: $R_m = \tilde{A}A$, where $\tilde{A}$ is the generalized inverse of A. For the GPS-only inversion, the matrix A is [*Barnhart and Lohman*, 2010]

$$A = \begin{pmatrix} WG \\ \beta S \end{pmatrix},$$

and for the joint GPS and aftershocks inversion it is

$$A = \begin{pmatrix} WG \\ \beta S \\ \gamma_\beta K \end{pmatrix}.$$

Singular value decomposition of A gives $A = U\Lambda V^T$ with U and V being orthogonal matrixes and Λ being a diagonal matrix of singular values. The generalized inverse of A is then $\tilde{A} = V\Lambda^{-1}U^T$. In calculating the inverse of Λ, I set to zero the reciprocal of singular values associated with unstable eigenvectors. Finally, the resolution matrix is $R_m = \tilde{A}A = (V\Lambda^{-1}U^T)(U\Lambda V^T)$.

[16] In previous geodetic-only studies of the 2004 Parkfield earthquake, the model fault has been discretized uniformly into no more than 300 elements [*Murray and Langbein*, 2006; *Langbein et al.*, 2006; *Johnson et al.*, 2006; *Barbot et al.*, 2009; *Page et al.*, 2009]. I have inverted the data with different number of cells (i.e., nonuniform quads) and found that the goodness of fit improves with increasing the number of cells up to about 1200, but it does not improve beyond that number. Such a large number of cells may seem to render the inversion even more underdetermined than the standard GPS-only inversion. Yet, a plot of the diagonal elements of the resolution matrix clearly shows that while the resolving power of the GPS inversion using 300 uniform cells drops quickly with distance from the GPS stations, such that the slip distribution below about 4 km and near the fault ends cannot be resolved (Figure 3a), the resolving power of the joint inversion using 1200 nonuniform cells is high both near the surface and in areas of aftershock activity at depths inaccessible to GPS-only inversions (Figure 3b). Thus, despite the factor of 3 increase in the number of elements, the resolution of the joint inversion is actually significantly better than that of the GPS-only inversion.

3.3. Evidence for Weak Dependency on Log of Slip Rate

[17] I have performed joint GPS-aftershocks inversions for different values of the friction constitutive parameter, a, and smoothing coefficient, β. In Figure 4 I show the percentage of residual between the model and the data as a function of β for different values of a. For comparison with results obtained for a uniform grid consisting of equal number of elements, I added the corresponding solution for $a = 10^{-4}$ (dashed line). Indeed the use of the quadtree approach results

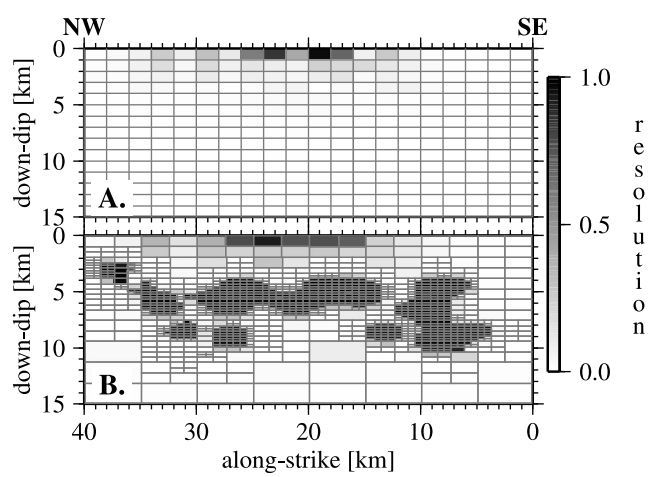

Figure 3. Model resolution. (a) The diagonal elements of the GPS-only resolution matrix calculated for a grid of 300 uniform cells. (b) The diagonal elements of the joint GPS-aftershocks resolution matrix calculated for a nonuniform grid of 1200 elements. In either case the resolution matrices were calculated for a smoothing coefficient corresponding to that of the preferred model (i.e., $\beta = 5 \times 10^{-5}$).

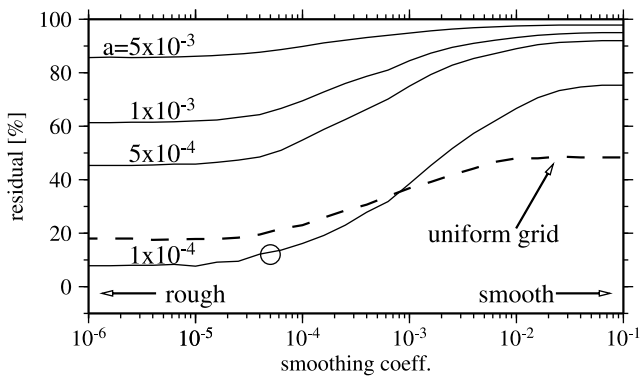

Figure 4. Misfit versus smoothness curves. Percentage of misfit between modeled and observed ground displacements as a function of the smoothing coefficient for different values of *a*. Dashed curve shows the result for a uniform grid consisting of 1200 cells and calculated for $a = 10^{-4}$. The circle indicates the preferred solution (see text).

in a substantially smaller residual. I find that the fits between the data set and the model improve upon decreasing the value of *a* and that more than 90% of data set may be fit with $a = 10^{-4}$. I conclude that the data are consistent with the Dieterich aftershock model. Yet while typical laboratory values for the friction parameter are in the range of 0.005 to 0.015 [*Dieterich and Kilgore*, 1996; *Scholz*, 1998], satisfactory fit to both aftershocks and GPS data sets can only be obtained for a constitutive friction parameter that is more than an order of magnitude lower than the laboratory values. Interestingly, a lower than experimental value of *a* parameter along the Parkfield segment has also been inferred by *Johnson et al.* [2006] based on afterslip modeling. I emphasis that the joint inversion provides an upper bound only on the frictional properties of fault patches that have experienced aftershock activity, but not elsewhere. Furthermore, that microearthquake activity is distributed nonuniformly and occupies only a small fraction of the Parkfield segment probably reflect nonuniform distribution of the frictional properties [*Waldhauser et al.*, 2004]. The frictional properties of the fault creeping areas may be constrained through modeling of the Parkfield afterslip [*Marone et al.*, 1991; *Johnson et al.*, 2006; *Johanson et al.*, 2006; *Barbot et al.*, 2009].

[18] Here I use a single value for the friction *a* parameter within the aftershocks zone. Alternatively, one could invert the data for nonuniform *a* parameter. In early stages of this study I have tried the following scheme: (1) set the *a* parameter to a value that is consistent with laboratory tests and solve for the slip distribution, (2) compute the stress misfit and half the *a* parameter on the aftershock patch having the largest misfit, (3) invert the data using the new *a* parameter distribution, and (4) repeat steps 2 and 3 until a target normalized misfit is reached. This test showed that a satisfactory fit to the data cannot be obtained unless the *a* parameter over most of the aftershocks zone is more than an order of magnitude lower than the experimental value, and therefore having a space-dependent friction parameter is not going to change the above conclusion.

[19] Recall that the earthquake catalog is more incomplete during the aftershock sequence than during the interseismic interval, and according to *Peng and Zhao* [2009] the number of aftershocks listed in the double-difference catalog that I use (and whose magnitude is greater than 1.5) is only 50%–60% of their actual number. It follows from equation (3) that the stress change derived from the aftershock rate change may be underestimated by about 30% on patches whose aftershock rate change is about 10, but only by 5% underestimated on fault patches where aftershock rate change is of the order of 10^5. Since these are the patches of largest aftershock rate that "push" the value of the *a* parameter well below the experimental value, the result of my calculation would have been affected only slightly had I used the more complete (but less well located) catalog of *Peng and Zhao* [2009], and in any case the $a = 10^{-4}$ that is needed here in order to satisfy 90% of the data should merely be regarded as an upper bound of the *a* parameter.

3.4. The Preferred Coseismic Slip Distribution

[20] I adhere to the conventional approach and regard as the preferred model the one that exhibits the smoothest slip distribution while satisfying most of the data (indicated by the circle in Figure 4). In Figure 1 I compare the observed and modeled ground motions and show the corresponding stress input, modeled stress and stress residual in Figure 5.

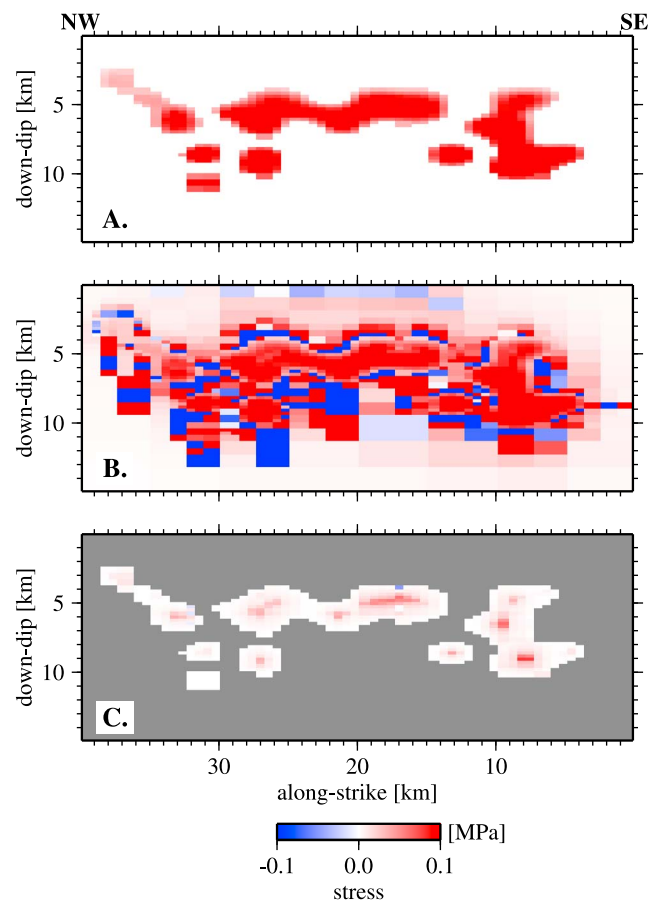

Figure 5. The preferred model stress maps. (a) Stress input that is calculated using equation (3) with $a = 10^{-4}$ and R^+/R^- distribution shown in Figure 2. (b) The stress distribution calculated from the modeled slip distribution. (c) The distribution of stress residual shown only for aftershock patches, with nonaftershock patches colored in grey.

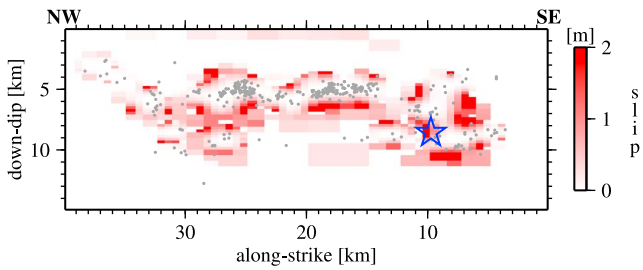

Figure 6. The preferred slip distribution. The abscissa starts at the southeast corner of the fault. Grey dots indicate the first day aftershocks. The star indicates the hypocenter.

The fit to either data set is about 90%. In Figure 6 I show the preferred model slip distribution. Note that the slip distribution is extremely nonsmooth, with the aftershock zones acting as barriers, i.e., areas of little coseismic slip (and large stress increase). The nonsmooth slip distribution that arises from my inversion is a consequence of the adopted aftershock model and the numerical grid. Given the irregular aftershock distribution, this slip distribution is what one would expect if the aftershocks occupied areas that experienced coseismic stress increase. For the solution to be consistent with fracture mechanics theory, the stress change due to slip plus the ambient stress should not exceed the host rock yield strength at a given depth. I inspected the stress distribution that results from the slip distribution in Figure 6 and verified that the above criterion is met. I therefore conclude that the slip distribution is physically sound.

[21] Unlike previous coseismic models of the Parkfield earthquake that utilize uniformly discretized fault and invert geodetic-only data [*Langbein et al.*, 2006; *Johanson et al.*, 2006; *Barbot et al.*, 2009], this model shows significant slip near the hypocenter (indicated by the blue star in Figure 6). Similar to a slip distribution inferred from GPS and strong motion data combined [*Custódio et al.*, 2009], the main slipping patch is long and narrow and is situated at a depth of about 6 km. In agreement with the seismological seismic moment, the geodetic moment magnitude of the preferred model is equal to 6.

3.5. Correlation Between Aftershock Distribution and Coseismic Stress Change Distribution

[22] In an attempt to gain insights regarding aftershock physics, studies that infer coseismic slip from geodetic and/or seismic data commonly examine whether aftershocks and coseismic slip distributions are correlated [*Custódio et al.*, 2009]. I now show that use of this approach, in cases where the inverse problem is underdetermined, may lead to an erroneous conclusion. I define as the fraction of discouraged aftershocks (FDA), the fraction of aftershocks that occurred in areas that have experienced coseismic stress decrease. In Figure 7 I show data misfit and FDA as a function of the smoothness coefficient for GPS-only (dashed) and joint GPS-aftershocks (solid) inversions, with the latter calculated using $a = 10^{-4}$. The smoothness of the preferred GPS-only inversion is between 10^{-4} and 10^{-3}, where the FDA is between 0.65 and 0.75, seemingly indicating that aftershock distribution within the study area is inconsistent with Dieterich's aftershock model. In contrast, inspection of the FDA obtained using the joint inversion clearly indicate that the vast majority of aftershocks (97%–99%) have occurred in areas that experienced coseismic stress increase. Thus the data are consistent with Dieterich's aftershock model being the dominant mechanism for aftershock production along the Parkfield segment. This conclusion is at odds with the two previous studies that addressed this issue [*Barbot et al.*, 2009; *Custódio et al.*, 2009].

4. Summary and Conclusions

[23] I describe a new approach for coseismic slip inversions, whereby both GPS displacements and first day aftershock rate changes are used jointly to constrain the solution. The joint inversion incorporates the Dieterich's aftershock model, which adopts a constitutive friction that depends logarithmically on the sliding rate. The method is applied to the 2004 Parkfield earthquake. Owing to the distance squared decay of the static displacement from the source, the spatial resolution provided by geodetic data alone decays rapidly with depth, and is thus limited to the upper few kilometers. On the other hand, the joint GPS-aftershocks inversion provides resolving power of slip at depths inaccessible to GPS-only inversions. Consequently, the slip distributions obtained using that method are much better constrained and may help to gain insight on the fault mechanical properties. For example, while other studies that inverted coseismic slip distributions first obtain a slip distribution that satisfies their data and then look for correlation with aftershock distribution, here the assumption that such a correlation exists is embedded into the slip inversion. By successfully fitting both GPS and aftershocks data sets, I

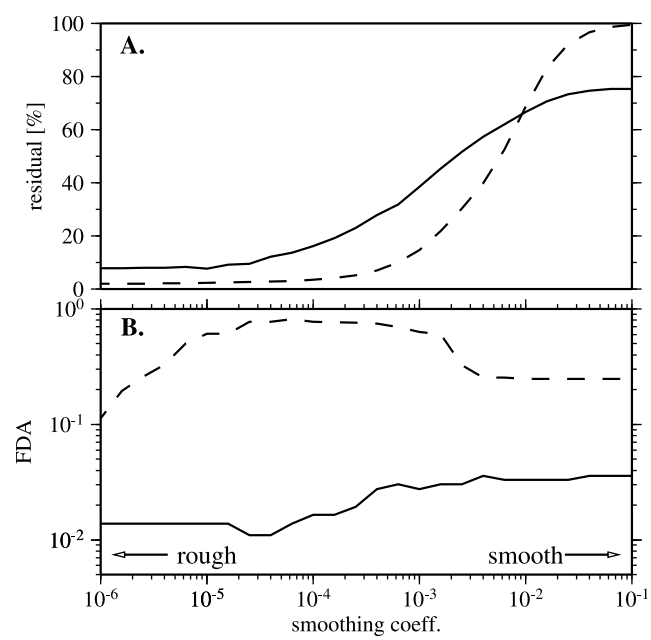

Figure 7. Testing the hypothesis that aftershock and coseismic stress change distributions are correlated. (a) Percentage of misfit as a function of smoothness coefficient. (b) Fraction of discouraged aftershocks (FDA) versus smoothness. Dashed and solid curves indicate solutions for GPS-only and joint GPS-aftershocks inversions, respectively, with the latter calculated using $a = 10^{-4}$.

show compatibility with the adopted aftershock model. I show that the joint inversion provides an upper bound on the friction dependence on the log of slip rate of fault patches that have experienced aftershock activity (but not elsewhere). Because rate- and state-dependent friction is being extensively adopted by probabilistic hazard assessments and the result of such calculations are dependent upon that parameter [*Toda et al.*, 1998; *Parsons et al.*, 2000; *Toda and Stein*, 2002], this conclusion is of great importance. Finally, the method presented here can be easily customized to include InSAR data and aftershocks occurring outside the rupture zone.

[24] **Acknowledgments.** I thank Budiman Minasny for providing the Quadtree computer code and Raul Madariaga for reviewing a draft of this manuscript. I thank the Associate Editor, an anonymous reviewer, and Roland Bürgmann for their constructive remarks.

References

Barbot, S., Y. Fialko, and Y. Bock (2009), Postseismic deformation due to the M_w 6.0 2004 Parkfield earthquake: Stress-driven creep on a fault with spatially variable rate-and-state friction parameters, *J. Geophys. Res.*, *114*, B07405, doi:10.1029/2008JB005748.

Barnhart, W. D., and R. B. Lohman (2010), Automated fault model discretization for inversions for coseismic slip distributions, *J. Geophys. Res.*, *115*, B10419, doi:10.1029/2010JB007545.

Bennington, N., C. Thurber, K. L. Feigl, and J. Murray-Moraleda (2011), Aftershock distribution as a constraint on the geodetic model of coseismic slip for the 2004 Parkfield earthquake, *Pure Appl. Geophys.*, *168*, 1553–1565, doi:10.1007/s00024-010-0214-x.

Budiman, M., A. B. McBratney, and J. J. Walvoort (2007), The variance quadtree algorithm: Use for spatial sampling design, *Comput. Geosci.*, *33*, 383–392, doi:10.1016/j.cageo.2006.08.009.

Chen, T., and N. Lapusta (2009), Scaling of small repeating earthquakes explained by interaction of seismic and aseismic slip in a rate and state fault model, *J. Geophys. Res.*, *114*, B01311, doi:10.1029/2008JB005749.

Custódio, S., M. T. Page, and R. J. Archuleta (2009), Constraining earthquake source inversions with GPS data: 2. A two-step approach to combine seismic and geodetic data sets, *J. Geophys. Res.*, *114*, B01315, doi:10.1029/2008JB005746.

Das, S., and K. Aki (1977), Fault plane with barriers: A versatile earthquake model, *J. Geophys. Res.*, *82*, 5658–5670.

Dieterich, J. H. (1979), Modeling of rock friction: 1. Experimental results and constitutive equations, *J. Geophys. Res.*, *84*, 2161–2168.

Dieterich, J. H. (1981), Constitutive properties of faults with simulated gouge, in *Mechanical Behavior of Crustal Rocks, Geophys. Monogr. Ser.*, vol. 24, edited by N. L. Carter et al., pp. 103–120, AGU, Washington, D. C.

Dieterich, J. H. (1994), A constitutive law for rate of earthquake production and its application to earthquake clustering, *J. Geophys. Res.*, *99*, 2601–2618.

Dieterich, J. H., and B. Kilgore (1996), Implications of fault constitutive properties for earthquake prediction, *Proc. Natl. Acad. Sci. U. S. A.*, *93*, 3787–3794.

Dieterich, J. H., V. Cayol, and P. Okubo (2000), The use of earthquake rate changes as a stress meter at Kilauea volcano, *Nature*, *408*, 457–460.

Du, Y., A. Aydin, and P. Segall (1992), Comparison of various inversion techniques as applied to the determination of a geophysical deformation model for the 1983 Borah Peak earthquake, *Bull. Seismol. Soc. Am.*, *82*, 1840–1866.

Fialko, Y., D. Sandwell, M. Simons, and P. Rosen (2005), Three-dimensional deformation caused by the Bam, Iran, earthquake and the origin of shallow slip deficit, *Nature*, *435*, 295–299, doi:10.1038/nature03425.

Gross, S., and R. Bürgmann (1998), Rate and state of background stress estimated from the aftershocks of the 1989 Loma Prieta, California, earthquake, *J. Geophys. Res.*, *103*, 4915–4928.

Helmstetter, A., G. Ouillon, and D. Sornette (2003), Are aftershocks of large Californian earthquakes diffusing?, *J. Geophys. Res.*, *108*(B10), 2483, doi:10.1029/2003JB002503.

Hsu Y. J., et al. (2006), Frictional afterslip following the 2005 Nias-Simeulue earthquake, Sumatra, *Science*, *312*, 1921–1926, doi:10.1126/science.1126960.

Johanson, I. A., E. J. Fielding, F. Rolandone, and R. Bürgmann (2006), Coseismic and postseismic slip of the 2004 Parkfield earthquake from space-geodetic data, *Bull. Seismol. Soc. Am.*, *96*, S269–S282, doi:10.1785/0120050818.

Johnson, K. M., R. Bürgmann, and K. Larson (2006), Frictional properties on the San Andreas fault near Parkfield, California, inferred from models of afterslip following the 2004 earthquake, *Bull. Seismol. Soc. Am.*, *96*, S321–S338, doi:10.1785/0120050808.

Kanamori, H., and G. Stewart (1978), Seismological aspects of Guatemala earthquake of February 4, 1976, *J. Geophys. Res.*, *83*, 3427–3434.

Langbein, J., J. R. Murray, and H. A. Snyder (2006), Coseismic and initial postseismic deformation from the 2004 Parkfield, California, earthquake, observed by Global Positioning System, electronic distance meter, creepmeters, and borehole strainmeters, *Bull. Seismol. Soc. Am.*, *96*, S304–S320, doi:10.1785/0120050823.

Lawson, C. L., and B. J. Hanson (1974), *Solving Least Squares Problems* Prentice-Hall, Englewood Cliffs, N. J.

Marone, C., C. H. Scholz, and R. Bilham (1991), On the mechanics of earthquake afterslip, *J. Geophys. Res.*, *96*, 8441–8452.

Mendoza, C., and S. Hartzell (1988), Inversion for slip distribution using teleseismic P waveforms: North Palm Springs, Borah Peak, and Michoacan earthquakes, *Bull. Seismol. Soc. Am.*, *78*, 1092–1111.

Murray, J., and J. Langbein (2006), Slip on the San Andreas fault at Parkfield, California, over two earthquake cycles, and implications for seismic hazard, *Bull. Seismol. Soc. Am.*, *96*, S283–S303, doi:10.1785/0120050820.

Nadeau, R. M., and L. R. Johnson (1998), Seismological studies at Parkfield VI: Moment release rates and estimates of source parameters for small repeating earthquakes, *Bull. Seismol. Soc. Am.*, *88*, 790–814.

Nadeau, R. M., W. Foxall, and T. V. McEvilly (1995), Clustering and periodic recurrence of microearthquakes on the San Andreas fault at Parkfield, California, *Science*, *267*, 503–507.

Ogata, Y. (1988), Statistical models for earthquake occurrences and residual analysis for point processes, *J. Am. Stat. Assoc.*, *83*, 9–27.

Okada, Y. (1992), Internal deformation due to shear and tensile faults in a half-space, *Bull. Seismol. Soc. Am.*, *82*, 1018–1040.

Page, M. T., S. Custódio, R. J. Archuleta, and J. M. Carlson (2009), Constraining earthquake source inversions with GPS data: 1. Resolution-based removal of artifacts, *J. Geophys. Res.*, *114*, B01314, doi:10.1029/2007JB005449.

Parsons, T., S. Toda, R. S. Stein, A. Barka, and J. H. Dieterich (2000), Heightened odds of large earthquakes near Istanbul: An interaction-based probability calculation, *Science*, *288*, 661–665.

Peng, Z., and Z. Zhao (2009), Migration of early aftershocks following the 2004 Parkfield earthquake, *Nat. Geosci.*, *2*, 877–881, doi:10.1038/ngeo697.

Rymer, M. J., et al. (2006), Surface fault slip associated with the 2004 Parkfield, California, earthquake, *Bull. Seismol. Soc. Am.*, *96*, S11–S27, doi:10.1785/0120050830.

Sammis, C. G., and J. R. Rice (2001), Repeating earthquakes as low-stress-drop events at a border between locked and creeping fault patches, *Bull. Seismol. Soc. Am.*, *91*, 532–537.

Scholz, C. H. (1998), Earthquakes and friction laws, *Nature*, *391*, 37–42.

Thurber, C., H. Zhang, F. Waldhauser, J. Hardebeck, A. Michael, and D. Eberhart-Phillips (2006), Three-dimensional compressional wavespeed model, earthquake relocations, and focal mechanisms for the Parkfield, California, region, *Bull. Seismol. Soc. Am.*, *96*, S38–S49, doi:10.1785/?0120050825.

Toda, S., and R. S. Stein (2002), Response of the San Andreas fault to the 1983 Coalinga-Nuñez earthquakes: An application of interaction-based probabilities for Parkfield, *J. Geophys. Res.*, *107*(B6), 2126, doi:10.1029/2001JB000172.

Toda, S., R. S. Stein, P. A. Reasenberg, J. H. Dieterich, and A. Yoshida (1998), Stress transferred by the 1995 M_w = 6.9 Kobe, Japan, shock: Effect on aftershocks and future earthquake probabilities, *J. Geophys. Res.*, *103*, 24,543–24,565, doi:10.1029/98JB00765.

Toda, S., R. S. Stein, and T. Sagiya (2002), Evidence from the AD 2000 Izu Islands swarm that stressing rate governs seismicity, *Nature*, *419*, 58–61.

Waldhauser, F., W. L. Ellsworth, D. P. Schaff, and A. Cole (2004), Streaks, multiplets, and holes: High-resolution spatio-temporal behavior of Parkfield seismicity, *Geophys. Res. Lett.*, *31*, L18608, doi:10.1029/2004GL020649.

Ziv, A. (2006a), What controls the spatial distribution of remote aftershocks, *Bull. Seismol. Soc. Am.*, *96*, 2231–2241, doi:10.1785/0120060087.

Ziv, A. (2006b), On the role of multiple interactions in remote aftershock triggering: The Landers and the Hector Mine case studies, *Bull. Seismol. Soc. Am.*, *96*, 80–89, doi:10.1785/0120050029.

A. Ziv, Department of Geophysics and Planetary Sciences, Tel Aviv University, Tel Aviv 69978, Israel. (zivalon@tau.ac.il)